Inferring the instability of a dynamical system from the skill of data assimilation exercises

Yumeng Chen[1], Alberto Carrassi[1,2,3], and Valerio Lucarini[3,4]

[1]Department of Meteorology and NCEO, University of Reading, UK
[2]Mathematical Institute, University of Utrecht, NL
[3]Centre for the Mathematics of Planet Earth, University of Reading, UK
[4]Department of Mathematics and Statistics, University of Reading, UK

Correspondence: Yumeng Chen (yumeng.chen@reading.ac.uk)

Abstract. Data assimilation (DA) aims at optimally merging observational data and model outputs to create a coherent statistical and dynamical picture of the system under investigation. Indeed, DA aims at minimizing the effect of observational and model error, and at distilling the correct ingredients of its dynamics. DA is of critical importance for the analysis of systems featuring sensitive dependence on the initial conditions, as chaos wins over any finitely accurate knowledge of the state of the system, even in absence of model error. Clearly, the skill of DA is guided by the properties of dynamical system under investigation, as merging optimally observational data and model outputs is harder when strong instabilities are present. In this paper we reverse the usual angle on the problem and show that it is indeed possible to use the skill of DA to infer some basic properties of the tangent space of the system, which may be hard to compute in very high-dimensional systems. Here, we focus our attention on the first Lyapunov exponent and the Kolmogorov-Sinai entropy, and perform numerical experiments on the Vissio-Lucarini 2020 model, a recently proposed generalisation of the Lorenz 1996 model that is able to describe in a simple yet meaningful way the interplay between dynamical and thermodynamical variables.

1 Introduction

1.1 Lyapunov vectors and related measures of chaos in a nutshell

The dynamics of the atmosphere or of the ocean are characterised by chaotic conditions, which, roughly speaking describes the property that a system has sensitivity to initial states. This means that, even in the presence of a perfect model, small errors in the initial conditions will grow in size with time, until the forecast becomes *de facto* useless (Kalnay, 2002)[1]. A mathematically-sound technique for studying the sensitivity to initial conditions of a system amounts to studying the properties of its tangent space. In particular, under fairly general mathematical conditions for a deterministic $n-$dimensional system whose asymptotic dynamics takes place in a compact attractor, one can define N Lyapunov exponents (LEs) $\lambda_1, \ldots, \lambda_N$, which are the asymptotic rates of amplification or decay of infinitesimally small perturbations with respect to a reference trajectory. Usually, the LEs are

---

[1]In the words of Ed Lorenz: "Chaos: When the present determines the future, but the approximate present does not approximately determine the future", see `https://tinyurl.com/faf3pnda`.

ordered according to their value, with λ_1 being the largest. Unless the system feature symmetries, all the LEs are distinct, and in the case of continuous time dynamics, one of them vanishes corresponding to the direction of the flow and defining the neutral tangent space. Once ordered from the largest to the smallest, the sum of the first k LEs gives the asymptotic growth rate of a $k-$volume element defined by k displaced infinitesimally nearby the reference trajectory plus the reference trajectory itself.

25   Additionally, if λ_{n_0} denotes the smallest non-negative LE, in many practical applications one can estimate the Kolmogorov-Sinai (or metric) entropy σ_{KS}, which defines the rate of creation of information of the system due to its instabilities, can be identified with $\sum_{i=1}^{n_0} \lambda_i$ (Pesin's identity). Finally, it is possible to use the spectrum of LEs to define a notion of dimension for the attractor of a chaotic systems. The Kaplan-Yorke conjecture, which follows from the estimate of the rate of growth of the infinitesimal $k-$volume, indicates that the information dimension of a chaotic attractor is given by $D_{KY} = p + \sum_{i=1}^{p} \lambda_i / |\lambda_{p+1}|$,

30   where p is the largest index such that $\sum_{i=1}^{p} \lambda_i \geq 0$. In systems where the phase space contracts (the large class of dissipative systems), one has $D_{KY} < n$. Roughly speaking, larger values of λ_1, of σ_{KS} and of D_{KY} are associated with conditions of high instability and low predictability for the flow. This is clearly an extremely informal presentation of some of the features and properties of the LE; see Eckmann and Ruelle (1985) for a now-classic discussion of these topics.

It is indeed possible to associate each LE with a physical mode. Ruelle (1979) proposed the idea of performing a covariant

35   splitting of the tangent linear space such that the basis vectors are actual trajectories of linear perturbations. The average growth rate of each of the covariant Lyapunov vector (CLVs) equals one of the LE. This idea was first implemented by Trevisan and Pancotti (1998) for studying the properties of the Lorenz 1963 model (Lorenz, 1963). Separate algorithms for the computation of CLVs were proposed in Ginelli et al. (2007) and Wolfe and Samelson (2007); see the recent comprehensive review by Froyland et al. (2013). Note that the CLVs corresponding to the positive (negative) LEs span the unstable (stable) tangent

40   space.

Recently, Lyapunov analysis of the tangent space was the subject of a special issue edited by Cencini and Ginelli (2013) and the book by Pikovsky and Politi (2016). Detailed Lyapunov analyses of geophysical flows on models of various levels of complexity have been recently reported (e.g., Schubert and Lucarini, 2015; Vannitsem and Lucarini, 2016b; Vannitsem, 2017; De Cruz et al., 2018b). Note that in many applications one might want to alter some of the aspects of the classical Lyapunov

45   analysis by accommodating for the study of how instabilities grow on a finite-time horizon (Palmer and Zanna, 2013) or of the growth of finite-size errors (Cencini and Vulpiani, 2013). In many applications, such non-asymptotic measures of error growth are more relevant than the classic Lyapunov analysis.

1.2   Data assimilation in chaotic systems: the signature and the use of chaos

Data assimilation (DA; Asch et al., 2016) refers to the family of theoretical and numerical methods that optimally combines

50   data with a dynamical model with the goal of improving the understanding of the phenomenon under study, enhancing the prediction skill, and quantifying the associated uncertainty. Data assimilation has long been studied and developed in the geosciences. It is an unavoidable piece of the operational numerical weather prediction workflow but it is nowadays used in a growing range of diverse areas of science (Carrassi et al., 2018).

Numerical evidences and recent analytical proofs have shown that, under certain conditions of the observations (their types,
spatio-temporal distribution, and accuracy), the performance of DA with chaotic dynamics relates directly to the instability
properties of the dynamical model where data are assimilated. One can thus in principle use the knowledge of the dynamical
features to inform not only the design of the DA that better suits the specific application - *e.g.*, how many model realizations
for the Monte Carlo based DA methods, the length of the assimilation window in variational DA - but also the best-possible
observational deployment.

A stream of research has shed light on the mechanisms driving the response of the ensemble-based DA (Evensen, 2009),
i.e. its functioning and suitability, when applied to chaotic systems. A recent comprehensive review can be found in Carrassi
et al. (2021), while we succinctly recall the main findings in the following. In the deterministic linear and Gaussian case with
Kalman filter (KF) and smoother (KS), it has been analytically proved that the error covariance matrices converge in time onto
the model's unstable–neutral subspace, *i.e.* the span of the backward Lyapunov vectors (BLVs), or of the covariant Lyapunov
vectors (CLVs), associated to the non-negative Lyapunov exponents (LEs, Bocquet et al., 2017; Bocquet and Carrassi, 2017).
These results have then been shown numerically to hold for the ensemble Kalman filter/smoother in weakly nonlinear regimes
(EnKF/EnKS; Evensen, 2009) by Bocquet and Carrassi (2017). In practice, for sufficiently well observed scenarios, the error
of the state estimate is fully confined within the unstable-neutral subspace. Because this subspace is usually much smaller
than the full system's phase space, the above convergence results imply that an ensemble size as large as the unstable-neutral
subspace dimension suffices to achieve satisfactorily performance, *i.e.* to track the "true" and effectively reduce the estimation
error thus leading to a substantial computational saving.

The picture slightly changes in the presence of a degenerate spectrum of LEs. This degeneracy often arises in systems with
multiple scales or in coupled dynamics (Vannitsem and Lucarini, 2016a; De Cruz et al., 2018a): the degeneracy usually regards
the unstable-neutral portion of the LE spectrum. In these cases it is necessary to increase the ensemble size to account for all
of the degenerate modes (Tondeur et al., 2020; Carrassi et al., 2021).

The necessity for going beyond the number of asymptotic unstable-neutral modes is also connected to the local variability of
the instantaneous instabilities along a system's trajectory. A recent study performed on a quasi-geostrophic model of the atmo-
sphere (Lucarini and Gritsun, 2020) provided a strong evidence that the large heterogeneity of the atmospherics's predictability
is due to the presence of substantial variability in the number of unstable dimensions (Lai, 1999) of the unstable periodic orbits
(UPOs) populating the attractor and defining the skeletal dynamics of the system (Auerbach et al., 1987). As a result of the fact
that the orbit of a chaotic system shadows the UPOs supported on the attractor in some of its regions , certain directions of the
stable space experience finite-time error growth due to locally important instabilities, causing the need for a larger ensemble
size than the dimension of unstable-neutral.

In the stochastic scenario, the above results still hold, although with some qualifications. Stochasticity usually injects noise
in the system irrespective of the flow-dependent modes of instabilities. Consequently, and with a non-zero probability, it also
injects error onto stable directions that would not have been otherwise influential in the long term. The trade-off between
the frequency of the noise injection and its amplitude on the one hand, and the dissipation rate of stable modes on the other,
determines the amplitude of the long term error along stable modes (Grudzien et al., 2018a). This mechanism implies the need

to include additional members in the ensemble to encompass weakly stable modes that experience instantaneous growth and,
90 although exacerbated by the presence of system noise, is present in any reduced-rank KFs as explained by Grudzien et al.
(2018b).

Moving away from the Gaussian and weakly-nonlinear scenario, the impact of instabilities on the functioning and performance of nonlinear DA, in particular particle filters (PFs, see *e.g.* Van Leeuwen et al., 2019) has also recently been clarified.
Carrassi et al. (2021) have shown that the number of particles needed to reach convergence depends on the size of the unstable-
95 neutral subspace rather than the observation vector size.

We have seen how the knowledge of the LEs and LVs can be used to operate key choices in the implementation of ensemble-
based DA schemes aimed at enhancing accuracy with the smallest possible computational cost. This view angle is made
explicit in a class of DA algorithms that operates a reduction in the dimension of the model (*e.g.*, the assimilation in the
unstable subspace, AUS, Palatella et al., 2013), of the data (Maclean and Van Vleck, 2021) or both (Albarakati et al., 2021).

100 ### 1.3 This paper: data assimilation as a tool to interrogate the dynamics

While extremely appealing from a theoretical view-point and practically useful in low-to-moderate dimensional problems, the
use of the dynamically informed DA approaches is difficult in high dimensions, where even just computing the asymptotic
spectrum of LEs, let alone the very relevant state-dependent local LEs (LLEs), is very difficult or just impossible. As pointed
out in Carrassi et al. (2021), the recent advent of powerful machine learning methods may open the path to efficiently emulate
105 the otherwise very costly recursive procedure to compute the LEs and vectors.

In this work, we attempt to reverse the view angle by posing the question: can we use the results of DA to infer some
fundamental quantities of the underlying dynamics, such as the spectrum of the LEs or the Kolmogorov-Sinai entropy (σ_{KS}),
that are, as aforementioned, difficult to compute in high-dimensions.

The paper is structured as the following: in Sect. 2, an upper bound of the root mean squared error of the Kalman filter for
110 the linear dynamics in the asymptotic limit is derived. In Sect. 3 we present the Vissio and Lucarini (2020) (VL20) model and
its DA setup. The VL 2020 model is a recently proposed generalisation of the Lorenz (1996) model that is able to describe
in a simple yet meaningful way the interplay between dynamical and thermodynamical variables. Additionally, the presence
of qualitatively distinct set of spatially extended variables allows one to consider non-trivial cases of partial observations for
DA exercises. Sect. 4 presents the main results of the paper by comparing the skill of the performed DA exercises with some
115 fundamental measures of instability of the VL20 model. Finally, in Sect. 5 we discuss our results and present perspectives for
future investigations.

2 Kalman filter error bounds and Lyapunov spectrum

We are interested in searching for a further relation between the skill of EnKF-like methods applied to perfect (no model error)
chaotic dynamics and the spectrum of LEs. We shall build our derivations on the results mentioned in Sect. 1.2 and reviewed in
120 Carrassi et al. (2021). In this section we set ourselves in a linear and Gaussian context, whereby the Kalman filter (KF) yields

the exact solution of the Gaussian estimation problem. Linear results will guide the interpretation of the findings in the general nonlinear setting with the EnKF.

At time t_k, let $\mathbf{x}_k \in \mathbb{R}^n$ and $\mathbf{y}_k \in \mathbb{R}^d$ be the state and observation vector, respectively. The (linear) model dynamics $\mathbf{M}_k \in \mathbb{R}^{n \times n}$ and observation model $\mathbf{H}_k \in \mathbb{R}^{p \times n}$ read

125
$$\mathbf{x}_k = \mathbf{M}_k \mathbf{x}_{k-1}, \tag{1}$$

$$\mathbf{y}_k = \mathbf{H}_k \mathbf{x}_k + \mathbf{v}_k. \tag{2}$$

The observation noise, $\mathbf{v}_k$, is assumed to be a zero-mean Gaussian white sequence with statistics

$$\mathrm{E}[\mathbf{v}_k \mathbf{v}_l^\top] = \delta_{k,l} \mathbf{R}_k, \tag{3}$$

with $\mathrm{E}[\ ]$ being the expectation operator, $\delta_{k,l}$ the Kronecker's delta function, and $\mathbf{R}_k$ the error covariance matrix of the observa-
130 tions at time t_k. For the sake of notation clarity, we assume that the model dynamics is non-degenerate so that all its Lyapunov exponents are distinct; we note that the extension to the general degenerate case is possible.

The singular vector decomposition (SVD) of the model dynamics between $t_k > t_l$ reads:

$$\mathbf{M}_{k:l} = \mathbf{U}_{k:l} \mathbf{\Lambda}_{k:l} \mathbf{V}_{k:l}^\mathrm{T}, \tag{4}$$

where $\mathbf{U}_{k:l}$ and $\mathbf{V}_{k:l}$ are non-degenerate orthogonal matrices and $\mathbf{\Lambda}_{k:l}$ the diagonal matrix of singular values. For $t_l \to -\infty$
135 the left singular vectors, $\mathbf{U}_{k:l}$, converge to the backward Lyapunov vectors (BLVs) at t_k, and, similarly for $t_k \to \infty$ the right singular vectors, $\mathbf{V}_{k:l}$, converge to the forward Lyapunov vectors (FLVs) at t_l. The singular values (SVs) in $\mathbf{\Lambda}_{k:l}$ converge to n distinct values of the form $\mathbf{diag}(\mathbf{\Lambda}_{k:l})_i = \exp(\lambda_i(t_k - t_l))$, in which λ_i are the Lyapunov exponents (LEs) in descending order, $\lambda_1 > \lambda_2 > \ldots \lambda_{n_0} = 0 > \lambda_{n-1} > \lambda_n$. The n_0 non-negative LEs identifies the n_0 unstable-neutral modes.

Let define the *information matrix*:

140
$$\mathbf{\Gamma}_k = \sum_{l=0}^{k-1} \mathbf{M}_{k:l}^{-\mathrm{T}} \mathbf{H}_l^\mathrm{T} \mathbf{R}_l^{-1} \mathbf{H}_l \mathbf{M}_{k:l}^{-1} = \sum_{l=0}^{k-1} \mathbf{M}_{k:l}^{-\mathrm{T}} \mathbf{\Omega}_l \mathbf{M}_{k:l}^{-1}, \tag{5}$$

which measures the "observability" of the state at t_k, with $\mathbf{\Omega}_l = \mathbf{H}_l^\mathrm{T} \mathbf{R}_l^{-1} \mathbf{H}_l$ being the *precision matrix* of the observations mapped to the model space. Moreover, let $\mathbf{U}_{+,k}^\mathrm{T}$ be a matrix whose columns are the n_0 unstable and neutral BLVs of the dynamics $\mathbf{M}_k$. Bocquet and Carrassi (2017) have shown that, if the following three conditions hold, **(i)** the unstable-neutral modes are sufficiently observed, such that

145
$$\mathbf{U}_{+,k}^\mathrm{T} \mathbf{\Gamma}_k \mathbf{U}_{+,k} > \epsilon \mathbf{I}_n \quad \epsilon > 0, \tag{6}$$

with $\mathbf{I}_n \in \mathbb{R}^n$ being the identity matrix, **(ii)**, the neutral modes, $\mathbf{u}$, are subject to the stronger constraint,

$$\liminf_{k \to \infty} \mathbf{u}_k^\mathrm{T} \mathbf{\Gamma}_k \mathbf{u}_k = \infty, \tag{7}$$

and, **(iii)** confining the initial error covariance matrix to the space of FLVs at time t_0, then the KF forecast error covariance matrix, $\mathbf{P}_k^f$, converges asymptotically to the sequence

$$\mathbf{P}_k = \mathbf{U}_{+,k}(\mathbf{U}_{+,k}^T \boldsymbol{\Gamma}_k \mathbf{U}_{+,k})^{-1}\mathbf{U}_{+,k}^T. \tag{8}$$

In real applications, the convergence (within numerical accuracy) occurs in long-but-finite times (Bocquet et al., 2017).

The asymptotic mean squared error of the forecast (MSEF) of the KF solution is given by the trace of Eq. (8),

$$n\text{MSEF} = \text{Tr}(\mathbf{P}_k) = \text{Tr}[\mathbf{U}_{+,k}(\mathbf{U}_{+,k}^T \boldsymbol{\Gamma}_k \mathbf{U}_{+,k})^{-1}\mathbf{U}_{+,k}^T] \tag{9}$$

$$= \text{Tr}[(\mathbf{U}_{+,k}^T \boldsymbol{\Gamma}_k \mathbf{U}_{+,k})^{-1}], \tag{10}$$

where, for last equality, we made use of the cyclic property of the matrix trace and the orthogonal relation of the BLVs, $\mathbf{U}_{+,k}^T \mathbf{U}_{+,k} = \mathbf{I}_{n_0}$. Equation (9) puts in evidence that the asymptotic MSEF depends on the observation constraint through the information matrix (data accuracy, encapsulated in $\mathbf{R}$, while data type and deployment encapsulated in $\mathbf{H}$) , but also on the unstable-neutral BLVs. Despite this, it is particularly involved to use Eq. (9) to derive a direct relation between the MSEF and the spectrum of LEs. This is because $\mathbf{U}_{+,k}$ is not invertible in general, and because one needs to make specific (often overly simplified) assumptions on the model dynamics and observations, *i.e.* on $\mathbf{M}_{k:l}$, $\mathbf{H}_l$ and $\mathbf{R}_l$, in order to get a treatable expression of the information matrix. In alternative, rather than a direct relation, we shall seek for informative bounds for the MSEF in terms of the LEs.

Let substitute the SVD of $\mathbf{M}_{k:l}$, Eq. (4), in the information matrix,

$$\boldsymbol{\Gamma}_k = \sum_{l=0}^{k-1} \mathbf{U}_{k:l}^{-T} \boldsymbol{\Lambda}_{k:l}^{-1} \mathbf{V}_{k:l}^{-1} \boldsymbol{\Omega}_l \mathbf{V}_{k:l}^{-T} \boldsymbol{\Lambda}_{k:l}^{-1} \mathbf{U}_{k:l}^{-1}. \tag{11}$$

For every t_l, the individual terms in the summation can be written as:

$$[\mathbf{U}_{k:l}\boldsymbol{\Lambda}_{k:l}\mathbf{V}_{k:l}^T \boldsymbol{\Omega}_l^{-1} \mathbf{V}_{k:l}\boldsymbol{\Lambda}_{k:l}\mathbf{U}_{k:l}^T]^{-1}. \tag{12}$$

We now define the maximum projection of the precision matrix onto the FLVs as:

$$\beta_l = \max_{\mathbf{h}\in\text{Im}(\mathbf{V}_{k:l}),\|\mathbf{h}\|=1} \mathbf{h}^T \boldsymbol{\Omega}_l^{-1} \mathbf{h}, \tag{13}$$

with $\|.\|$ being the Euclidean norm, and use it to get an upper bound for the inverse of each term, Eq. (12), in the information matrix summation,

$$\mathbf{U}_{k:l}\boldsymbol{\Lambda}_{k:l}\mathbf{V}_{k:l}^T \boldsymbol{\Omega}_l^{-1} \mathbf{V}_{k:l}\boldsymbol{\Lambda}_{k:l}\mathbf{U}_{k:l}^T \leq \beta_l \mathbf{U}_{k:l}\boldsymbol{\Lambda}_{k:l}^2 \mathbf{U}_{k:l}^T. \tag{14}$$

The inequality is based on the Löwner partial ordering of $\mathbb{R}^{n\times n}$ (*i.e.* the partial order defined by the convex cone of positive semi-definite matrices; see *e.g.*, Bocquet et al. (2017) their Appendix B). We shall use this partial ordering in the following derivations.

175   By defining the maximum of β_l across all $0 \leq t_l \leq t_{k-1}$ as

$$\beta_k = \max_{l=0,\ldots,k-1} \beta_l, \tag{15}$$

we get the following lower bound for the information matrix:

$$\beta_k^{-1} \sum_{l=0}^{k-1} (\mathbf{U}_{k:l} \mathbf{\Lambda}_{k:l}^2 \mathbf{U}_{k:l}^{\mathrm{T}})^{-1} \leq \sum_{l=0}^{k-1} [\mathbf{U}_{k:l} \mathbf{\Lambda}_{k:l} \mathbf{V}_{k:l}^{\mathrm{T}} \mathbf{\Omega}_l^{-1} \mathbf{V}_{k:l} \mathbf{\Lambda}_{k:l} \mathbf{U}_{k:l}^{\mathrm{T}}]^{-1} \tag{16}$$

$$= \mathbf{\Gamma}_k. \tag{17}$$

180   The bound reflects the effect of assimilating observations (the rhs) compared to the unconstrained free model run (the lhs) -
note that $\mathbf{U}_{k:l} \mathbf{\Lambda}_{k:l}^2 \mathbf{U}_{k:l}^{\mathrm{T}} = \mathbf{M}_{k:l} \mathbf{M}_{k:l}^{\mathrm{T}}$.

Given that $\mathbf{U}_{k:l} \mathbf{\Lambda}_{k:l}^2 \mathbf{U}_{k:l}^{\mathrm{T}}$ is symmetric positive definite, we can invoke the aforementioned partial ordering for this class of
matrices, and further develop the lower bound of the information matrix as

$$\mathbf{U}_{k:l} \mathbf{\Lambda}_{k:l}^2 \mathbf{U}_{k:l}^{\mathrm{T}} \leq e^{2\lambda_1(t_k - t_l)} \mathbf{I} = \mathbf{D}_l, \tag{18}$$

185   where $e^{2\lambda_1(t_k - t_l)}$ is the largest eigenvalue of $\mathbf{U}_{k:l} \mathbf{\Lambda}_{k:l}^2 \mathbf{U}_{k:l}^{\mathrm{T}}$. The lower bound of the information matrix in Eq. (16) then
becomes

$$\beta_k^{-1} \sum_{l=0}^{k-1} \mathbf{D}_l^{-1} \leq \mathbf{\Gamma}_k. \tag{19}$$

Under the assumption that the assimilation cylcle is uniform in time, e.g. $\Delta t = t_k - t_{k-1} = t_{k-1} - t_{k-2} = \cdots = t_1 - t_0$, the
summation of the diagonal matrices $\mathbf{D}_l^{-1}$ coincides with a geometric series with known sums:

190   $$s_i^{-1} = \sum_{l=0}^{k-1} \mathbf{D}_{l,ii}^{-1} = \begin{cases} \dfrac{e^{-2\lambda_1 \Delta t} - e^{-2\lambda_1(k+1)\Delta t}}{1 - e^{-2\lambda_1 \Delta t}} & \lambda_1 > 0 \\ k & \lambda_1 = 0 \end{cases}. \tag{20}$$

By using the lower bound, Eq. (19), and the orthogonality of the BLVs, $\mathbf{U}_{+,k}^{\mathrm{T}} \mathbf{U}_{+,k} = \mathbf{I}_{n_0}$, we get a lower bound for the
information matrix projected onto the unstable-neutral subspace:

$$\beta_k^{-1} s_i^{-1} \mathbf{I}_{n_0} = \beta_k^{-1} s_i^{-1} \mathbf{U}_{+,k}^{\mathrm{T}} \mathbf{I}_n \mathbf{U}_{+,k} \leq \mathbf{U}_{+,k}^{\mathrm{T}} \mathbf{\Gamma}_k \mathbf{U}_{+,k}. \tag{21}$$

We can thus finally use Eq. (21) in the expression of the MSEF, Eq. (9), and derive the following upper bound:

195   $$n\mathrm{MSEF} = \mathrm{Tr}[(\mathbf{U}_{+,k}^{\mathrm{T}} \mathbf{\Gamma}_k \mathbf{U}_{+,k})^{-1}] \tag{22}$$

$$\leq \mathrm{Tr}(\beta_k s_i \mathbf{I}_{n_0}) \tag{23}$$

$$= \beta_k \sum_{i=1}^{n_0} \frac{1 - e^{-2\lambda_1 \Delta t}}{e^{-2\lambda_1 \Delta t} - e^{-2\lambda_1(k+1)\Delta t}} \tag{24}$$

$$\rightarrow \beta_k \sum_{i=1}^{n} \frac{1 - e^{-2\lambda_1 \Delta t}}{e^{-2\lambda_1 \Delta t}} \quad k \rightarrow \infty \tag{25}$$

$$= \beta_k n_0 (e^{2\lambda_1 \Delta t} - 1). \tag{26}$$

200 This upper bound incorporates the key players shaping the relation between the KF estimation error and the model dynamics.
The presence of β_k and Δt reflects the observation modulation of the MSEF: the stronger the data constraint the smaller β_k
and Δt. The signatures of the model instabilities are in the term n_0, the size of the unstable-neutral subspace, and in λ_1, the
error growth rate along the leading mode of instability, both related directly to the amplitude of the bound. Under a Bayesian
interpretation, the factor β_k can be seen as the likelihood of data, and the remaining terms in the bound altogether as the prior
205 distribution. Note that, if the dynamical model is stable (and independently of the data), $\lambda_1 = 0$, $s_i = \frac{1}{k}$ and the MSEF goes to
zero asymptotically.

   As alluded at the beginning of the section, a direct expression (*e.g.* an equality in place of a bound) relating the model insta-
bilities and the error can be obtained under strong simplified and somehow unrealistic assumptions on the form of the model
dynamics and of the data. For example, if the linear dynamics $\mathbf{M}$, the observation covariance matrix $\mathbf{R}$, and the observation
210 operator $\mathbf{H}$ are all scalar matrices. With no need of those assumption, and with more generality, the upper bound, Eq. (26),
indicates that the MSEF is determined by a convolution of model dynamics and observation error.

   In the next sections we will perform numerical experiments under controlled scenarios to investigate the conditions for which
the bound holds. In particular, we will study the conditions leading to the smallest possible upper bound, such that the output
of a converged DA, *i.e.* its asymptotic MSEF, can be used to infer the LEs spectrum of the model dynamics.

215 ## 3 Experimental setting

3.1 The Vissio-Lucarini 2020 model

Our test-bed for numerical experiments is the low-order model recently developed by Vissio and Lucarini (2020), hereafter
referred to as the VL20. The VL20 model is an extension of the classical Lorenz 96 model (Lorenz, 1996) that includes
additional thermodynamic variables. The model is given by the following set of n ODEs (with n being an even integer):

$$\frac{\mathrm{d}X_i}{\mathrm{d}t} = X_{i-1}(X_{i+1} - X_{i-2}) - \alpha\theta_i - \gamma X_i + F \tag{27}$$

$$\frac{\mathrm{d}\theta_i}{\mathrm{d}t} = X_{i+1}\theta_{i+2} - X_{i-1}\theta_{i-2} + \alpha X_i - \gamma\theta_i + G \tag{28}$$

where X represents the momentum, θ is the thermodynamic variable, and the subscript $1 \leq i \leq n/2$ is the gridpoint index. The
model is spatially periodic, and the boundary condition is expressed as:

$$X_{i-n/2} = X_{i+n/2} = X_i \tag{29}$$

225 $$\theta_{i-n/2} = \theta_{i+n/2} = \theta_i \tag{30}$$

   In the VL20 model it is possible to introduce a notion of kinetic energy $K = \sum_{=1}^{n/2} X_j^2/2$ and potential energy $P = \sum_{=1}^{n} X_j^2/2$. Additionally, the model features an energy cycle that allows for the conversion between the kinetic and poten-
tial forms and for introducing a notion of efficiency. The parameter α modulates the energy transfer between the two forms,
while γ controls the energy dissipation rate and F and G are external forcing defining the energy injection into the system.

Table 1. Instabilities features of the VL20 model for the three forcing configurations; $n = 36$, and $\alpha = \gamma = 1$.

(F, G)	(10, 10)	(10, 0)	(0, 10)
λ_1	1.587	1.340	1.475
n_0	10	7	10
σ_{KS}	6.248	3.917	6.103
D_{KY}	20.037	15.742	19.510

The model's evolution can be written as the sum of a quasi-symplectic term, which conserves the total energy, and of a gradient term, which describes the impact of forcing and dissipation. In the turbulent regime, the VL20 allows for propagation of signals in the form of wave-like disturbances associated with unstable waves exchanging energy in both potential and kinetic form with the background. In terms of energetics, the difference between the L96 and the VL20 model mirror the one between a one-layer and a two-layer quasi-geostrophic model, because the former features only barotropic processes, while the latter, features the coupling between dynamical and thermodynamic processes via baroclinic conversion, which makes its dynamics much more complex (Holton and Hakim, 2013). The VL20 model is thus a very good test-bed for research in DA, a further step toward realism from the very successful L96. Further details on the model as well as an extensive analysis of its dynamical and statistical properties can be found in Vissio and Lucarini (2020).

In all the following experiments, we set $n = 36$ implying both model variables X and θ have 18 components, and consider three model configurations differing in the values of the external forcings: $F = G = 10$, $F = 10, G = 0$, and $F = 0, G = 10$. Unless otherwise stated, the model runs with the default parameters $\alpha = \gamma = 1$, and it is numerically integrated using the standard 4-th order Runge-Kutta time stepping method with a time step $\Delta t = 0.05$ time units. A summary of the model instability properties with the chosen configurations is given in Tab. 1.

3.2 Data assimilation setup

Synthetic observations are generated according to Eq. (2) by sampling a "true" solution of the VL20 model, Eqs. (27), and then adding simulated observational error from the Gaussian distribution $\mathcal{N}(\mathbf{0}, \mathbf{R})$. Observational error is assumed to be spatially uncorrelated thus that the error covariance, $\mathbf{R}$, is a diagonal matrix, and we observe the model components directly, implying that the observation operator is linear and under the form of a matrix, $\mathbf{H} \in \mathbb{R}^{p \times n}$. The observation error variance is set to be 5% of the variance (*i.e.* the squared temporal variability) of the climatology of the corresponding state vector component such that:

$$diag(\mathbf{R})_i = 5\% Var(X), i = 1, \ldots, \frac{n}{2}; \tag{31}$$

$$diag(\mathbf{R})_i = 5\% Var(\theta), i = \frac{n}{2} + 1, \cdots, n. \tag{32}$$

By linking the observation error to the model variance makes the setup more realistic, but it ties the error amplitude to the choice of the model parameters. For example, the model's state vector variance gets very small when the dissipation is strong,

255 potentially making the $\mathbf{R}$ matrix degenerate. Under such circumstances, the corresponding entries in $\mathbf{R}$ are set to 5×10^{-6}.

In line with previous studies (*e.g.*, Carrassi et al., 2021), we work with deterministic EnKFs, whereby it is possible to study the filter performance in relation to the model instabilities without the inclusion of additional noise that is inherent to stochastic versions of the EnKFs (Evensen, 2009). In particular we choose to use the finite-size ensemble Kalman filter (EnKF-N, Bocquet et al., 2015) because it automatically computes the required covariance inflation thus saving us from running many inflation

260 tuning experiments. The initial conditions for the ensemble are sampled from the Gaussian distribution $\mathcal{N}(\mathbf{x}_0^t, \mathbf{R})$ with the $\mathbf{x}_0^t$ being the "truth" at t_0: this choice signigies that the initial condition error is taken to be equal to the observational error.

The performance of DA experiments will be assessed primarily by using the root mean square error of the analysis, normalised by the observation variance:

$$\text{nRMSEa} = \sqrt{\frac{1}{n}\left(\frac{\sum_{i=1}^{n/2}(X_i - X_{i,truth})^2}{diag(R)_i} + \frac{\sum_{i=1}^{n/2}(\theta_i - \theta_{i,truth})^2}{diag(R)_{i+n/2}}\right)}. \tag{33}$$

265 The nRMSEa measures the analysis error independent from observation error, allowing for a multivariate assessment of the performance. Unless otherwise stated, observations are taken at every time step, and the experiments last $2,000$ model time units. With this setting, an experiment comprises $40,000$ DA cycles, and when computing time-averages of the nRMSEa, we only consider the last 500. Finally, and again unless otherwise stated, we shall adopt $N = 40$ ensemble members in the EnKF-N.

4 Numerical results

Our analysis focuses on the relation between observational design and filter accuracy, and the relation between the model instabilities and the filter accuracy. By exploiting the novel dynamical-thermodynamical feature of VL20 over its L96 precursor, we will also study the EnKF-N under observational scenarios that alternatively measure the dynamical variable, $\mathbf{X}$, or, the thermodynamical one, $\boldsymbol{\theta}$.

4.1 Data assimilation with the VL20 model: general features

Fig. 1 shows the time series of the nRMSEa over the first 100 time units, for the three main model configurations under consideration. In all cases, the error drops to below 20% of the observational error after approximately 10 time units (corresponding to 200 DA cycles), and then fluctuates with oscillations that only sporadically lead the error to exceed 0.3. The configuration, $(F, G) = (10, 0)$ (red line), attains the smaller error, while the other two configurations (blue and green lines respectively) show

280 comparable error levels slightly larger than configuration $(F, G) = (10, 0)$. Recall that in the configuration of $(F, G) = (10, 0)$, the model is not thermodynamically forced ($G = 0$), and is also slightly stabler than in the other two configurations (*cf.* Tab. 1).

The first connection between the filter performance and the model instabilities is drawn from Fig. 2 that shows the nRMSEa as a function of the number of the ensemble members. In line with previous findings for uncoupled univariate (Bocquet and
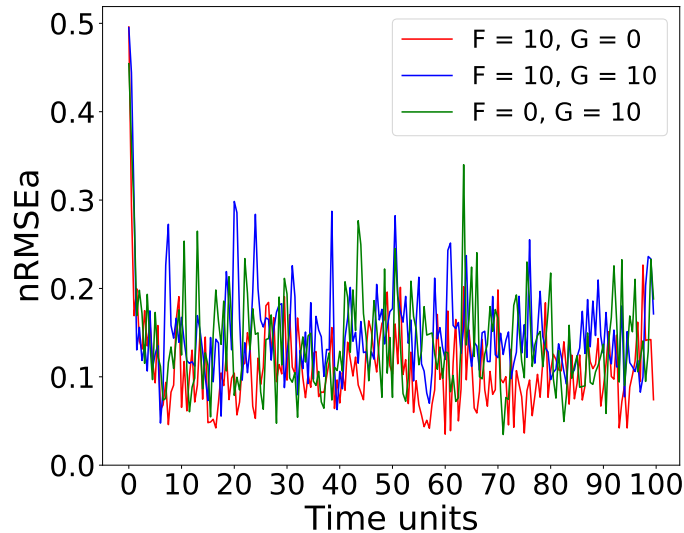
Figure 1. Time series of nRMSEa over the first 100 time units ($2,000$ DA cycles) using $\alpha = \gamma = 1$ on $n/2 = 18$ grid points with an ensemble size of $N = 40$.

Carrassi, 2017) and with coupled models (Tondeur et al., 2020), Fig. 2 shows that, even with a multivariate model, the error

285 converges to very low level as soon as the ensemble size exceeds the number of unstable-neutral modes, n_0, and that it does not further decreases by adding more members. This behaviour is possible because error evolution is bounded to be linear or weakly nonlinear. This means that one can in principle induce linearity intentionally in the error evolution to meet the aforementioned relation between filter accuracy and ensemble size and use it to infer the number of unstable-neutral modes. In a DA experiment, a "practical" way to achieve this is by strengthening the observational constraint (*i.e.*, by increasing the

290 measurements spatial and temporal density); here we observe the full system's state at every time-step.

 The VL20 model represents four main physical mechanisms: i) the transition from kinetic to potential energy; ii) the energy injection from external forcing; iii) the advection; and iv) the dissipation. Although these processes all participate the evolution of the model with nonlinear interplay's that cannot be straightforwardly disentangled, we shall try to refer to them when interpreting the outcome of the DA experiments. In particular, in each experiment we will attempt to identify the prevailing

295 mechanism over the aforementioned four. We perform three experiments, where we observe the full system state (*i.e.*, $\mathbf{H} = \mathbf{I}_{36}$), or alternatively $\mathbf{X}$ or $\boldsymbol{\theta}$ alone (implying in both cases $\mathbf{H} \in \mathbb{R}^{18 \times 36}$). Results are given in Fig. 3, that displays the time averaged nRMSEa (global or for the dynamics or thermodynamics only) over a range of the coefficient α that modulates the energy transfer rate.

 Overall, and as expected, the analysis error is smaller in the observed variables (*cf* the left and mid columns and corre-

300 sponding color lines), and attains the smallest level when $\mathbf{X}$ and $\boldsymbol{\theta}$ are simultaneously observed (right column). Nevertheless a few remarkable points can be raised. First, when the system is fully observed, for large α (*i.e.* for large conversion between available potential energy and kinetic energy) the skills in $\mathbf{X}$ and $\boldsymbol{\theta}$ get very similar (right column): we conjecture this to be
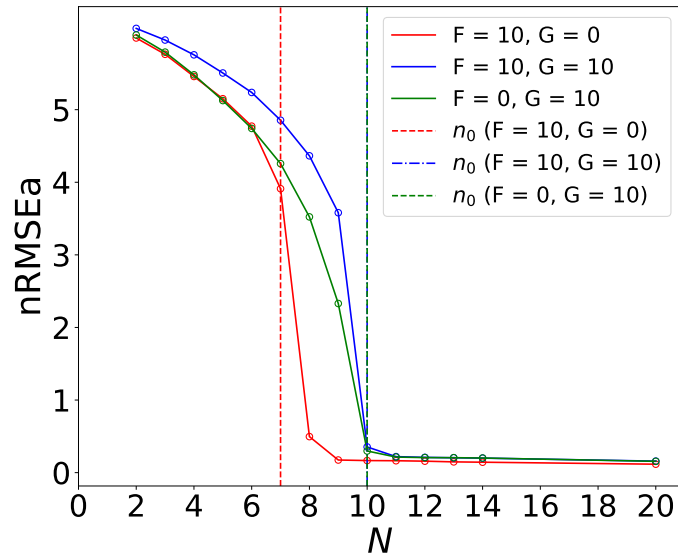
Figure 2. The time-averaged nRMSEa for all experiment configurations. The vertical dashed lines indicate the dimension of unstable-neutral subspace, n_0. The n_0 under the forcing $F = 10, G = 10$ is the same as the forcing condition $F = 0, G = 10$, which shows overlapped vertical lines. For the sake of numerical errors, the neutral mode is chosen as the LE that is closest to 0.

a consequence of the system getting more evenly turbulent with all variables sharing a similar internal variability as energy is exchanged efficiently between the kinetic and potential form. Second, for small α (*i.e.*, small energy conversion), the effect of external forcing becomes dominant and determines the analysis error of $\mathbf{X}$ and $\boldsymbol{\theta}$ (last column in Fig. 3). For instance, whenever the momentum is externally forced ($F = 10$), the error in $\mathbf{X}$ is systematically smaller than in $\boldsymbol{\theta}$ (first and second rows of the last column): DA is more effective in controlling the dynamics than the thermodynamics even when they are subject to the same observational constraint. The situation is somehow reversed when only the thermodynamics is forced ($F = 0, G = 10$): the analysis error of the momentum and the thermodynamic variable is undifferentiated. With small α and no forcing for the momentum, the nonlinear momentum advection is limited by the small magnitude of the momentum that is not able to activate much the dynamical variables, so that we observe similar analysis error between the thermodynamics variable and the momentum.

Finally, the effect of the energy transfer and advection can be revealed by looking at the partially observed experiments (left and mid columns). Both mechanisms involve the momentum, making it more efficacious to observe $\mathbf{X}$ than $\boldsymbol{\theta}$ especially in the energy transfer dominated regime (large α). However, in an advection-dominated regimes (small α), if $\boldsymbol{\theta}$ is unobserved, $\mathbf{X}$ has limited capability to constrain the error in $\boldsymbol{\theta}$ due to the weak feedback from $\boldsymbol{\theta}$ to $\mathbf{X}$. On the other hand, observing $\boldsymbol{\theta}$ reduces error in $\mathbf{X}$ via the accurate estimate of the advection process of $\boldsymbol{\theta}$ (see mid column).

Further insight on the role of the driving (unstable) variable, and on the interplay between the prevailing physical mechanisms and the analysis error is given by looking at the CLVs (Kuptsov and Parlitz, 2012). In Fig. 4 we show at (normalized time-
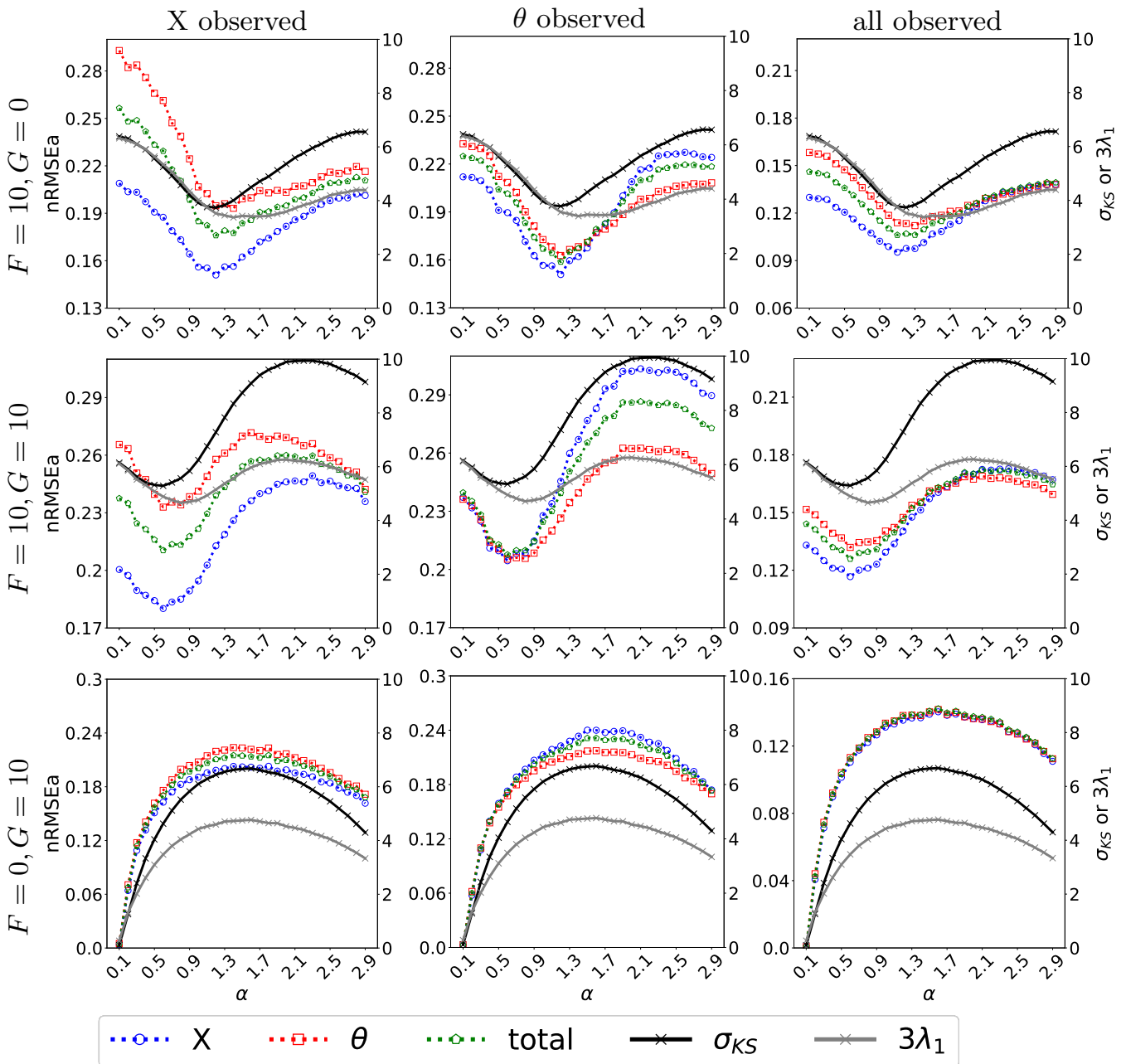
Figure 3. The nRMSEa with varying energy transfer coefficient $\alpha \in (0, 3)$ (with an interval of 0.1) and dissipation coefficient $\gamma = 1$. The left axis represents nRMSEa while the right axis shows the σ_{KS} and the λ_1 scaled by a factor of 3. The results come from perfect model assumption with observations at each time step where all variables, only X/θ is observed.
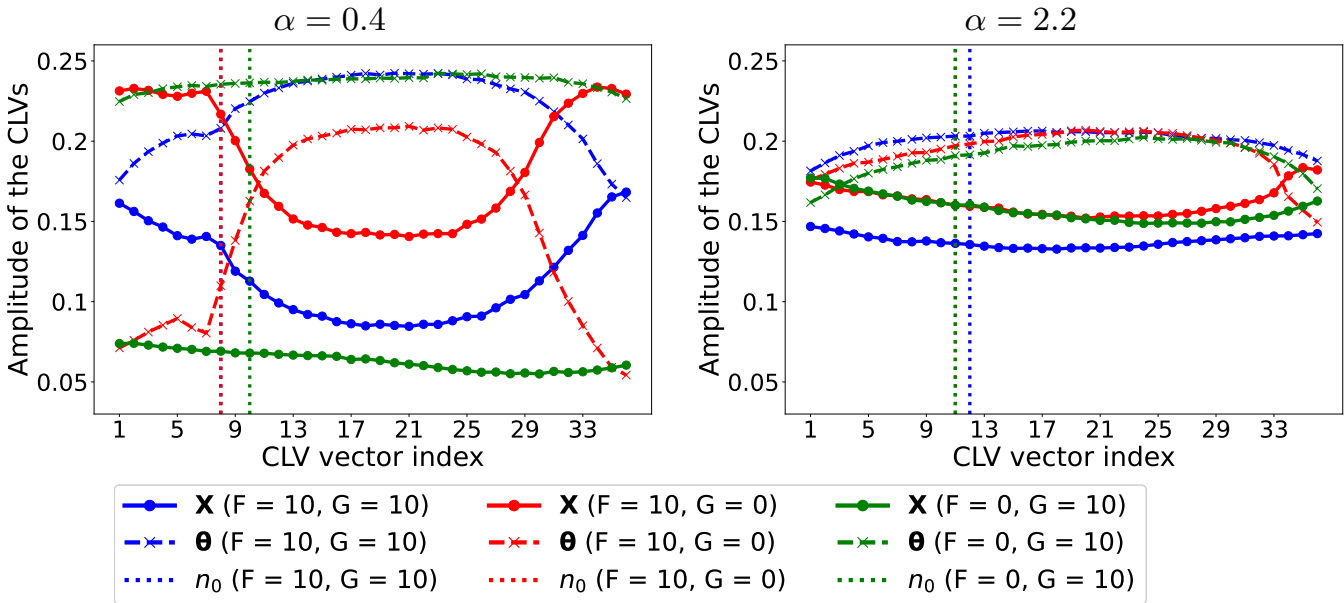
Nonlinear Processes
in Geophysics
Discussions

Figure 4. Normalized time-averaged amplitude of CLV components (the absolute value) for $\alpha = 0.4$ and $\alpha = 2.2$. In both cases $\gamma = 1$. The vertical lines indicate the corresponding dimension of the unstable-neutral subspace, n_0.

320   averaged) absolute amplitude of CLVs components along the state vector: it tells us which variables/component have the larger influence on each CLVs, thus indicating what processes participate more to a specific direction of error growth/decay.

As discussed above, the change of α induces the shift from the advection dominated regime to an energy mixing one, where the thermodynamics and the kinetic energy mixes with each other: these two regimes are portrayed in Fig. 4, by selecting $\alpha = 0.4$ and $\alpha = 2.2$. Moreover, these two values of α correspond roughly to those giving the largest differences in nRMSEa

325   between the momentum and the thermodynamic variables (*cf* left and mid panels of Fig. 3). For small energy exchange ($\alpha = 0.4$ - left column in Fig. 4), the model instabilities are driven by the external forcing, with the driving variable being the one where energy is injected. This is clearly visible when comparing the amplitudes of CLVs between **X** and $\boldsymbol{\theta}$ on the left column of Fig. 4: larger amplitudes of the unstable-neutral CLVs are found in the forced variables. When the momentum and the thermodynamics are equally forced (blue lines), the amplitude of the unstable-neutral CLVs for **X** and $\boldsymbol{\theta}$ are close to each other.

330   The nonlinear advection process intensifies the error growth, especially for **X**. The nonlinear advection and the momentum is of lesser importance if the momentum is not forced ($F = 0, G = 10$ - green lines) while the thermodynamic processes control dominantly both the stable and unstable subspace. The thermodynamic variable on the stable subspace acts as an energy sink to stabilize the dynamical system. The effect of the thermodynamics is shown noticeably by the large relative amplitude of the CLVs of the thermodynamic variable in the stable subspace when the momentum is directly forced ($F = 10$ - blue and red

335   line).

The situation changes sensibly when the energy exchange is the dominant physical mechanism ($\alpha = 2.2$ - right column). This causes a stronger mixing across the model variables so that both **X** and $\boldsymbol{\theta}$ play a comparable role in the unstable-neutral

components of the CLVs leading to similar amplitude of the CLVs for all types of forcing. Remarkably, the effect of the energy conversion also applies to the stable components of the CLVs leading to similar amplitude of the CLVs between $\mathbf{X}$ and $\boldsymbol{\theta}$.

340   The results in Fig. 4 reveal the effect of the prevailing physical mechanisms on determining the driving unstable variables. The figure suggests what variables should in principle be controlled by targeting measurements on the portion of the system's state vector with larger amplitude on the unstable-neutral CLVs.

Along with α, the energy in the system is modulated by the dissipation, γ: larger values of γ implies an efficient removal of energy from the system, and thus reducing the system's variability of both the potential and kinetic energy. At dynamical
345   level, the parameter γ controls the contraction of the phase space as the sum of all Lyapunov exponents (equal to the average flow divergence) is $-n\gamma$. Hence, one expects that larger values of γ correspond to weaker instability for the model, as in the case of the classical L96 model (Gallavotti and Lucarini, 2014). Fig. 5 is the same as Fig. 3 but for the dissipation, γ. Overall, we see that, with large γ, the system's internal variability reduces and we find similar small errors in both $\mathbf{X}$ and $\boldsymbol{\theta}$. For weaker dissipation, the momentum is better controlled than the thermodynamics. With partial observations (left and
350   mid columns), the error is much larger than in the corresponding fully observed cases. Similar to Fig. 3, the momentum is generally better reconstructed by the DA than the thermodynamics, although observing the latter appears more efficacious (*i.e.* it leads to smaller analysis error) than observing the momentum. We think that this is due to the prevailing mechanism being the advection of the thermodynamics given that $\alpha = 1$ in these experiments (*cf.* also Fig. 3). The amplitudes of the CLVs along the state vector is studied in Fig. 6. We consider the cases $\gamma = 0.4$ and $\gamma = 1.0$ for which the difference in the nRMSEa between
355    $\mathbf{X}$ and $\boldsymbol{\theta}$ is roughly the largest (*cf* Fig. 5).

With the leading CLVs strongly affected by the external forcing, the amplitude of the CLVs along the system's components is similar to the pattern of low energy exchange rate in Fig. 4 where $\alpha = 0.4$ even though here, $\alpha = 1$. This confirms that the dynamical regime of our experiments lies in the regime dominated by advection, and dissipation does not mix the kinetic and potential energy diffusely as the energy exchange, but rather it uniformly removes both types of energy without changing the
360   prevailing physical mechanism. This is also reflected in the consistently low nRMSEa for the observed variable when varying dissipation rates in the partially observed experiments (see Fig. 5). The decreasing analysis error in Fig. 5 corresponds to the increases of γ, which reduces the dimension of the unstable-neutral subspace with increased relative importance of forced variables in the unstable-neutral subspace as the fast energy removal reduce the amount of energy mixing.

The results of Sect. 4.1 confirm the relation between the performance of DA (in terms of analysis error) and the dimension
365   and characteristics of the unstable-neutral subspace. In particular, we conclude that successful DA relies on controlling the error in the unstable-neutral subspace by observing the variable that drives the error growth. The VL20 model enabled the investigation of the relation between the DA and the specific physical mechanisms such as the advection, the energy transfer among dynamics and thermodynamics as well as the dissipation. The effect of DA (*i.e.* its efficacy) is strongly influenced by the form of the coupling between the unobserved and the observed variables that is in turn shaped by the prevailing physical
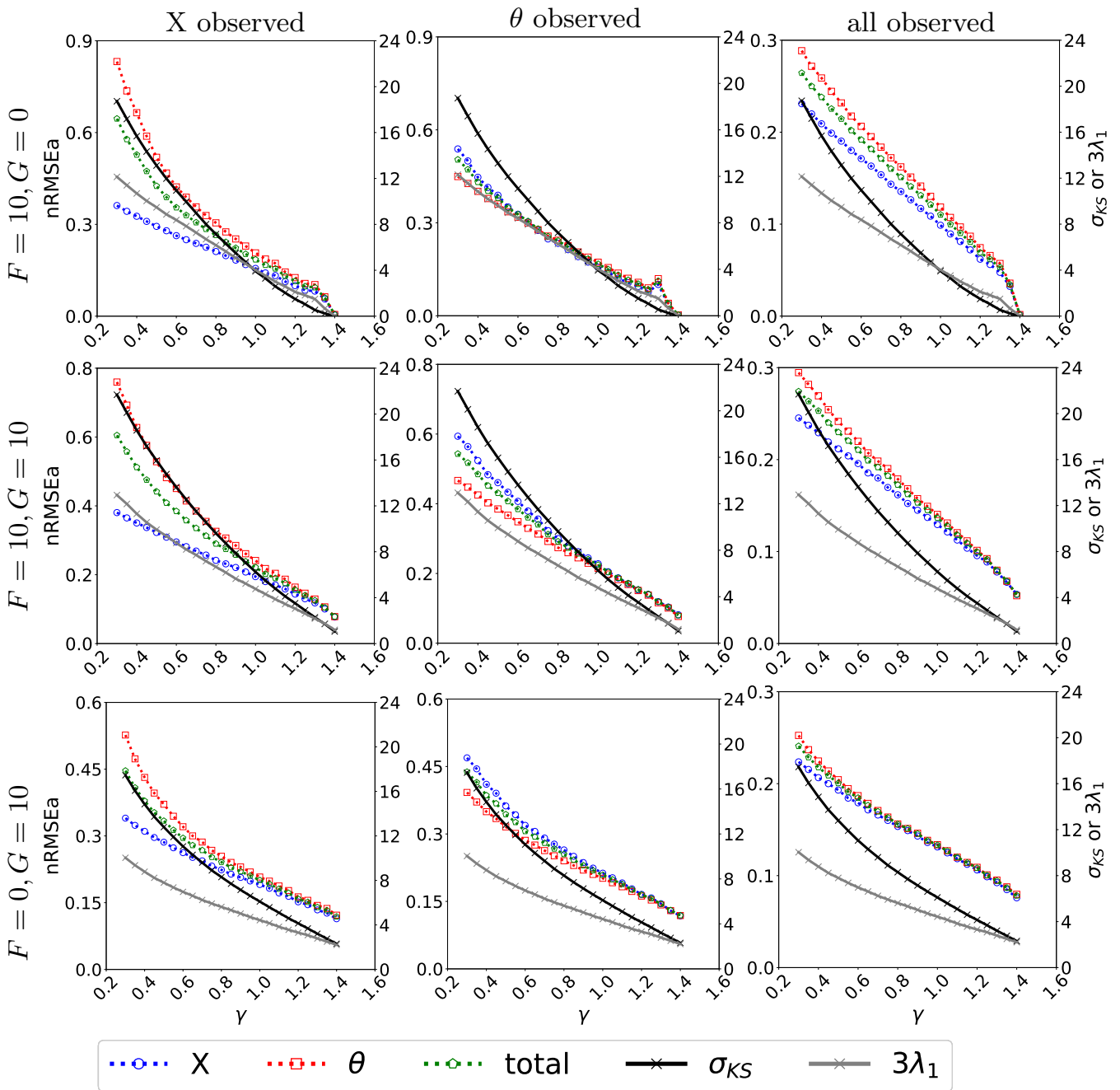370   mechanisms.

15

Figure 5. The nRMSEa with varying dissipation coefficients $\gamma \in [0.3, 1.8]$ (with an interval of 0.05) and $\alpha = 1$. The left axis represents nRMSEa while the right axis shows the σ_{KS} and λ_1 scaled by a factor of 3. The results come from perfect model assumption with observations at each time step where all variables, only X/θ is observed exists.
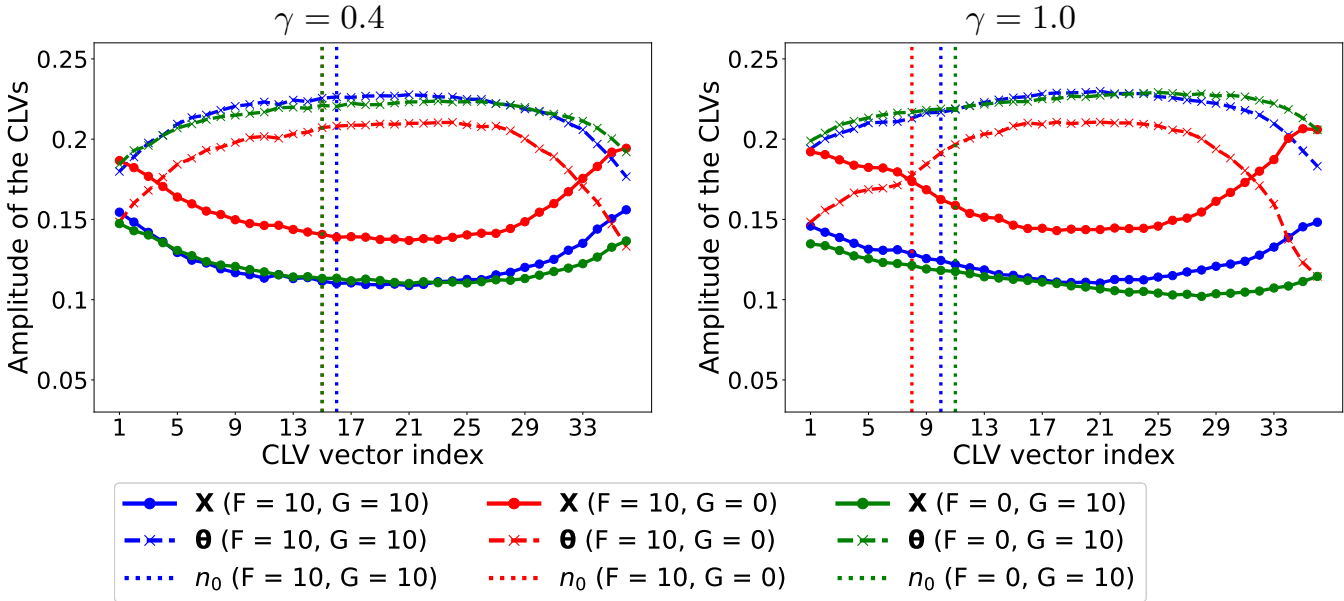
Figure 6. Normalized time-averaged amplitude of CLV components for $\gamma = 0.4$ and $\gamma = 1$ with $\alpha = 1$. The vertical lines indicates the dimension of the unstable-neutral subspace.

4.2 Inferring the degree of model instability with data assimilation

The derivation in Sect. 2 shows that, in the linear setting, the assimilation error is asymptotically bounded from above by a factor dependent on the observation error, the first LE and the number of unstable-neutral modes of the underlying forecast model. In this section we explore the extent to which this result holds in a nonlinear scenario whereby the observational constraint is strong enough such that the error evolution is maintained approximately linear or weakly-nonlinear. We shall make use of numerical experiments with the VL20 model.

A first insight on the existence of a direct relation between the model instabilities and the skill of the EnKF-N is already provided in Fig. 3 and 5. They display the Kolmogorov-Sinai entropy, σ_{KS} (black line) and the first LE, λ_1 (amplified by a factor of 3 - gray line), along with the nRMSEa (discussed in Sect. 4.1). Even just by visual inspection the figures clearly evidence the high correlation between the analysis error and both the σ_{KS} and λ_1.

The nature of this relation is further studied in Fig. 7 that shows scatter plots between the nRMSEa (with black markers) and σ_{KS}/λ_1 in a log-log scale. Points are relative to experiments the forcing values given in the panels' legends and with varying energy exchange and dissipation rates in the range $(\alpha \times \gamma) \in [0.1, 3) \times [0.3, 1.8)$. Here, the EnKF-N assimilates the full state vector at each time step. The analysis error appears in a linear relationship with either σ_{KS} or λ_1, as long as $\ln(\text{nRMSEa}) \geq -4$. The existence of such a quasi-linear relationship provides the possibility to infer σ_{KS} and/or λ_1 based on the outcome of DA.
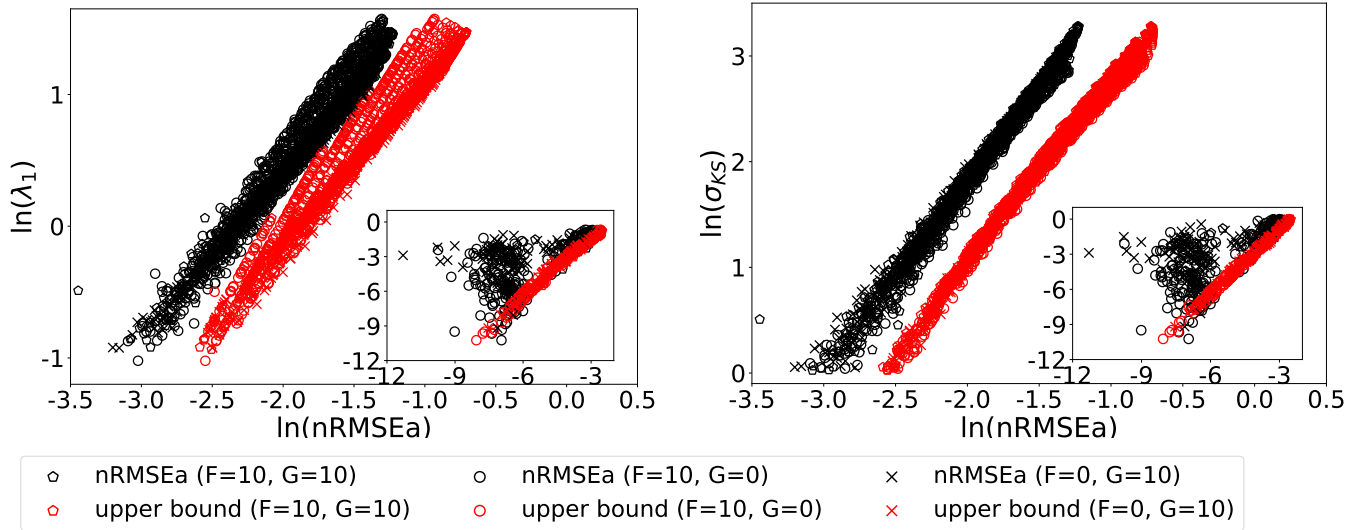
Figure 7. Scatter plots of λ_1 (left) and σ_{KS} (right) against the nRMSEa for experiments with observations of the entire state vector at each time step. The theoretical analysis error upper bound are also displayed (red markers). The log scale is used on both axes. The experiments use the model forcing given in the legend and the energy rate and dissipation in the range $(\alpha \times \gamma) \in [0.1, 3) \times [0.3, 1.8)$ with an interval of 0.1×0.05. The stable configurations ($\sigma_{KS} < 1$) have been excluded. The inset shows the weakly unstable model configurations ($0 < \sigma_{KS} \leq 1$).

The scatter plots also demonstrate the validity of the upper bound (red markers) of Eq. (26) in Sect. 2. To compute the bound we set the coefficient related to observation, $\beta = 1$, as it is compared to analysis errors that normalized by observational error. The nRMSEa is bounded by the theoretical upper bounds for most of the model configurations considered. The spread of upper

390 bounds points for given λ_1 (left panel) reflect the various values of n_0 under similar λ_1. The better correspondence (narrower spread of the scattered points) in the plane $nRMSEa$ with σ_{KS} (right panel) shows the importance of including both the dominant error growth rate, λ_1, and the unstable-subspace dimension, n_0, - both present in σ_{KS} - to better characterise the system's instabilities. The correspondence between σ_{KS} and the theoretical upper bound could also be a result of the relation between λ_1 and σ_{KS} as in highly turbulent case, there is a linear relation between λ_1 and σ_{KS} in (Gallavotti and Lucarini,

395 2014).

The linear relation does not hold when $\ln(\text{nRMSEa}) < -4$ (see the black markers distribution in the panels' inset). We explain this behaviour in the following way. The wide clouds of points in correspond all to model configurations with very small σ_{KS} and λ_1. In these quasi-stable dynamics, the error growth in between successive analysis is very little, with occasional error decay. The observational error, which is random and white-in-time, will be often larger than the forecast error and will

400 dominate the analysis error, thus breaking its direct dependence on the instability-driven forecast error. In addition, in the weakly unstable model configurations, the most unstable direction behaves almost like a neutral mode which also breaks the
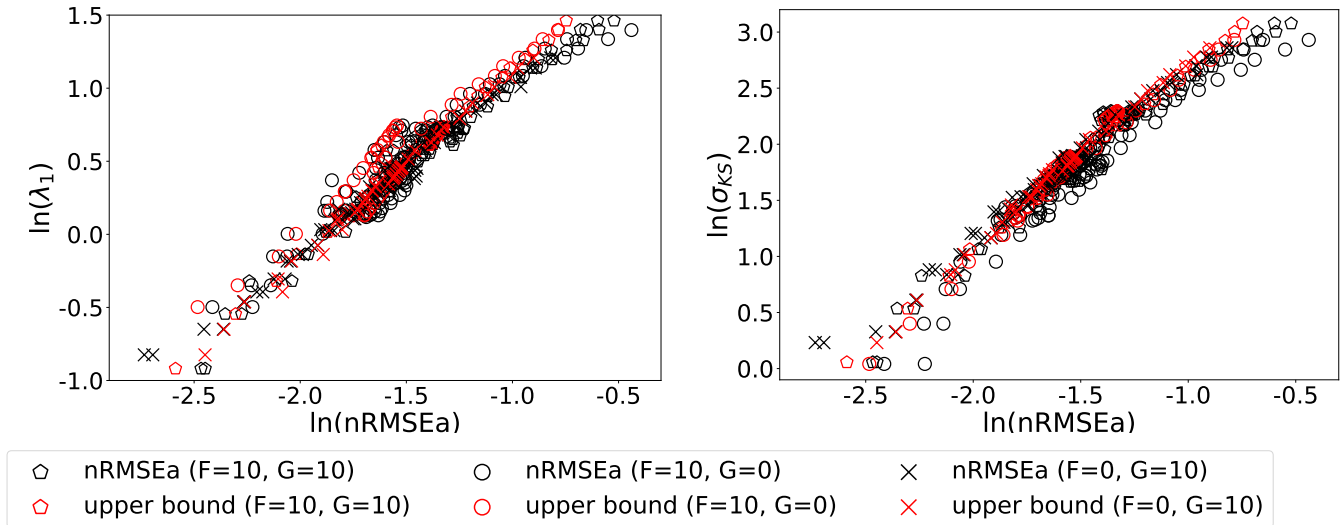
Figure 8. Scatter of σ_{KS} (left) and λ_1 (right) against nRMSEa for experiments where either the momentum or the thermodynamic variable alone is observed. The log-log scale is used in both axes, and points represent experiments with the same model parameter values used in Fig. 3 and 5, excluding weakly unstable cases with $\sigma_{KS} < 1$, and hence excluding cases where $\ln(\text{nRMSEa}) < -4$ similar to Fig. 7.

assumptions of the theoretical upper bound for unstable models. In fact, we do not show the weakly unstable results with $\sigma_{KS} < 1$ for both σ_{KS} and λ_1.

The error bounds in Sect. 2 relies on the assumption of linear error evolution, a condition that we met in our experiments

405 thanks to a strong observational constraint, with (synthetic) measurements covering the full state vector at each time-steps. These conditions are rarely achievable in practice, so it is relevant to explore how results will change with lighter observational constraint. There are three direct ways to achieve this by acting on (i) the number/type of measurements, (ii) the measurement error, and/or, (iii) the temporal frequency.

The effect of the first is studied in Fig. 8 that is similar to Fig. 7 but for DA experiments whereby only one of each variable

410 in the VL20 is observed.

The impact of partially observing the system causes the emergence of a weakly quadratic relationship between the analysis error and either σ_{KS} or λ_1. However, the analysis error is still uniquely and monotonically related to them especially for σ_{KS}. A quadratic law requires one additional coefficient to be determined compared to a linear law, yet the mere existence of such a law suggests again that one could in principle infer σ_{KS} and/or λ_1 based on the analysis error. With the relaxed observation

415 constraint, the analysis error can (and indeed do so in several instances) exceed the theoretical upper bound. However, the general trend of the numerical experiments still follow the theoretical upper bound.

We study the effect of changing the amplitude of the observational error in Fig. 9. Results reveal that varying the observation error in the range of $5\% - 10\%$ does not break the quasi-linear relationship between the analysis error and σ_{KS} or λ_1. The nRMSEa is quite insensitive to the observation variance due to the normalization. Nevertheless, the upper bound is not violated
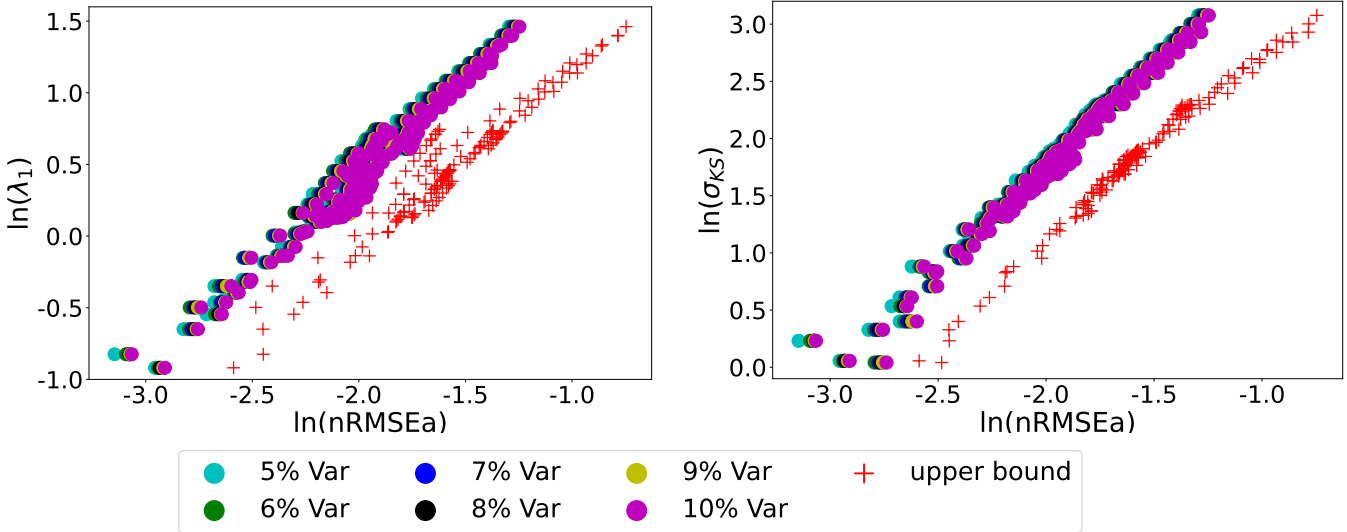
Nonlinear Processes
in Geophysics

Open Access

EGU

Discussions

Figure 9. Scatter plots of σ_{KS} (left) and λ_1 (right) against nRMSEa. The log-log scale is used on both axes. The different points refer to experiments with different observation error given in the legend and model parameter as in Fig. 3 and 5 and excluding weakly unstable cases with $\sigma_{KS} < 1$, and hence excuding cases where $\ln(\text{nRMSEa}) < -4$ similar to Fig. 7.
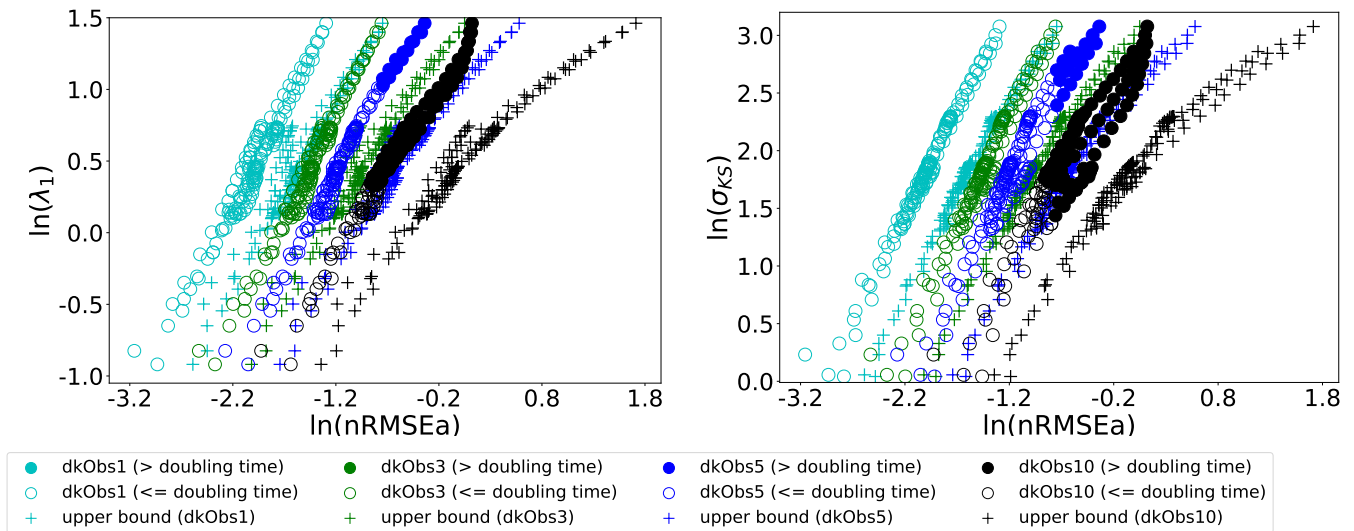
Figure 10. Scatter plots of σ_{KS} (left) and λ_1 (right) against nRMSEa. The log-log scale is used on both axes. The different points refer to experiments with different observation interval given in the legend and model parameter as in Fig. 3 and 5 and excluding cases when $\sigma_{KS} < 1$. The filled circle represents the cases where the observation interval exceeds the doubling time of the error.

420   as in Fig. 7 and the slope of the nRMSEa from the numerical experiment is remarkably similar to the slope of the theoretical bound.

Finally, the impact of varying the observation frequency is explored in Fig. 10. It is patent that decreasing the frequency leads to blurring the linear relation between the analysis error and the σ_{KS} or λ_1. There is a clear deviation from the trend of the theoretical upper bound and from the uniqueness of the relation between analysis error and σ_{KS}, as soon as the observational

425   time interval exceeds the error doubling time (that is inverse related to λ_1), and DA error evolves beyond the linear regime. However, for frequent enough observations a linear relation similar to the upper bound appears and, again, one could in principle deduce σ_{KS} and/or λ_1 based on DA.

Finally note that, the different effect of the observational noise and data frequency depicted in Fig. 9 and Fig. 10 is consistent with the findings in Bocquet and Carrassi (2017) (their appendix) where it is shown how observation frequency is a much more

430   effective driver to induce (or to break) linear error evolution.

5   Conclusions

It is sometimes of great importance to be able to obtain information on the instability of a system of interest by performing data analysis of suitably defined observables. This is of key importance when one does not have direct access to the evolution equations of the system or when the analysis of its tangent space is too computationally burdensome. As an example, quanti-

435   tative information on the degree of instability of a chaotic system can be extracted using extreme value theory by studying the statistics of close dynamical recurrences as well as of extremes of so-called physical observables (Lucarini et al., 2014, 2016). The use of such a strategy has shown a great potential for the analysis of geophysical fluid dynamical models in a highly turbulent regime (Gálfi et al., 2017) as well for the understanding of the properties of the actual atmosphere (Faranda et al., 2017; Messori et al., 2017).

440   In this study, we have addressed this problem by taking the angle of DA. The relation between DA and the instability of the dynamical system where it is applied has long been studied (see *e.g.* Miller et al., 1994; Carrassi et al., 2008), and has been used to design DA techniques in various field of geosciences (Carrassi et al., 2021; Albarakati et al., 2021). Here, we have reversed this viewpoint and investigated the possibility of using DA to infer fundamental quantities of the underlying dynamics, in particular the Lyapunov exponents, λ_i, or the Kolmogorov-Sinai entropy (σ_{KS}). The basic idea is to look at DA as a control

445   problem, and relate our ability to control the system, *ceteris paribus*, to its underlying instability. We have leveraged on a stream of previous works that set the theoretical foundation and that proved the convergence of the error covariance of the Kalman filters onto the unstable-neutral subspace of the dynamical system. Based on this, we derived here an upper bound of the Kalman filter forecast error, *i.e.* under the assumptions of a linear model dynamics and a linear observation operator. The upper bound is very informative as it relates the error's amplitude to all of the essential descriptors of the model instabilities

450   on the one hand and of the DA on the other. These are the dimension of the unstable-neutral subspace, n_0, the first Lyapunov exponent, λ_1, the frequency of the observation assimilation, Δt, and the observation error, β_k. By properly normalising the bound by the observation error, it can be written as a function of the model dynamical properties exclusively.

The existence of a relation between λ_1 or σ_{KS} and the DA skill, as well as the validity of the bound, has then been investigated in a nonlinear scenario using numerical experiments. We have used the EnKF-N (Bocquet et al., 2015) as a prototype of

455   deterministic EnKF (Evensen, 2009) and the new model developed by Vissio and Lucarini (2020). The VL20 is an extension
of the widely used Lorenz 96 model that includes a thermodynamic component. While maintaining all of the virtues of a low-
dimensional model suitable for investigations on new methods at low computational cost, VL20 is conceptually much richer
than the original L96 model. In particular it allows for the exchange of energy between a kinetic and potential form, which,
together with forcing and dissipation, provides the fundamental framework for the Lorenz (1955) energy cycle. Additionally,

460   as advection impacts temperature-like variables, one can observe the emergence of more complex dynamical behaviors. By
changing the value of its key parameters, and in particular of those determining its forcing and dissipation, the model explores
various dynamical regimes, ranging from fixed point, periodic, quasi-periodic, and chaotic behaviour. In terms of DA, the
VL20 model has the attractive feature that it includes two qualitatively different set of variables, associated with dynamics and
thermodynamics, respectively. Hence, it is possible to explore the problem of having partial observation beyond focusing of

465   the spatial extent of the observations only.

We demonstrate that the skill of the EnKF-N is directly linked to both λ_1 and σ_{KS}. Whenever the error within the EnKF-N
cycles are kept sufficiently linear via a strong observational constraint, the relation is clearly linear too. By relaxing the ob-
servational constraint (by either reducing the frequency of measurements or by increasing their noise) deviation from linearity
emerge. Nevertheless, the linear relation is very robust against the level of observational noise (within certain range) while it

470   turns quadratic once the interval between successive measurements gets too large and it exceeds the system's doubling time.
Similarly, we found out that the theoretical upper bounds for the errors, derived for linear system, still holds as long as the
observational constraint is strong enough, but are then violated.

The error bound and the linear relation between error and λ_1 and σ_{KS} represent a potentially powerful direct way to infer
λ_1 and σ_{KS} by looking at the output of a DA exercise. Knowing the analysis error (or a suitable approximate estimate of it)

475   computing σ_{KS} or λ_1 requires the unstable-neutral subspace dimension, n_0. It can be obtained by looking at the analysis error
convergence when increasing the ensemble size, N: n_0 will be equal to $N^* - 1$ where N^* being the smallest ensemble size for
which the error reaches is minimum.

There are some follow up questions that emerge naturally from this work. Among those, we are currently considering how
these results will change when performing DA for state and parameter estimation. In this context, a relevant recent study has

480   shown how the minimum number of ensemble members, N^*, will need to be increased to include as many members as the
number of parameters to be estimated (Bocquet et al., 2020). By modifying its parameters, the model's instabilities properties
will change too, potentially inducing a catastrophic change (a tipping point) of its long term behavior. Data assimilation will
then need to infer the best parameter values to track the data signal and keep the DA solution on its same region of the
bifurcation diagram.

485   *Code availability.* The Python script for the plotting and data assimilation experiments is available at https://github.com/yumengch/InferDynPaper,
which also is dependent on version 1.1.0 of the Python package DAPPER (https://github.com/nansencenter/DAPPER/releases/tag/v1.1.0).

References

Albarakati, A., Budišić, M., Crocker, R., Glass-Klaiber, J., Iams, S., Maclean, J., Marshall, N., Roberts, C., and Van Vleck, E. S.: Model
and data reduction for data assimilation: Particle filters employing projected forecasts and data with application to a shallow water model,
Computers & Mathematics with Applications, 2021.

Asch, M., Bocquet, M., and Nodet, M.: Data assimilation: methods, algorithms, and applications, SIAM, 2016.

Auerbach, D., Cvitanović, P., Eckmann, J.-P., Gunaratne, G., and Procaccia, I.: Exploring chaotic motion through periodic orbits, Phys. Rev.
Lett., 58, 2387–2389, https://doi.org/10.1103/PhysRevLett.58.2387, 1987.

Bocquet, M. and Carrassi, A.: Four-dimensional ensemble variational data assimilation and the unstable subspace, Tellus A: Dynamic Mete-
orology and Oceanography, 69, 1304 504, 2017.

Bocquet, M., Raanes, P. N., and Hannart, A.: Expanding the validity of the ensemble Kalman filter without the intrinsic need for inflation,
Nonlinear Processes in Geophysics, 22, 645–662, https://doi.org/10.5194/npg-22-645-2015, 2015.

Bocquet, M., Gurumoorthy, K. S., Apte, A., Carrassi, A., Grudzien, C., and Jones, C. K. R. T.: Degenerate Kalman Filter Error
Covariances and Their Convergence onto the Unstable Subspace, SIAM/ASA Journal on Uncertainty Quantification, 5, 304–333,
https://doi.org/10.1137/16M1068712, 2017.

Bocquet, M., Farchi, A., and Malartic, Q.: Online learning of both state and dynamics using ensemble Kalman filters, Foundations of Data
Science, https://doi.org/10.3934/fods.2020015, 2020.

Carrassi, A., Ghil, M., Trevisan, A., and Uboldi, F.: Data assimilation as a nonlinear dynamical systems problem: Stability and convergence
of the prediction-assimilation system, Chaos: An Interdisciplinary Journal of Nonlinear Science, 18, 023 112, 2008.

Carrassi, A., Bocquet, M., Bertino, L., and Evensen, G.: Data assimilation in the geosciences: An overview of methods, issues, and perspec-
tives, Wiley Interdisciplinary Reviews: Climate Change, 9, e535, 2018.

Carrassi, A., Bocquet, M., Demaeyer, J., Gruzien, C., Raanes, P., and Vannitsem, S.: Data assimilation for chaotic dynamics, in: Data
Assimilation for Atmospheric, Oceanic and Hydrologic Applications (Vol. IV), edited by Park, S. K. and Xu, L., Springer International
Publishing, Switzerland, 2021.

Cencini, M. and Ginelli, F.: Lyapunov analysis: from dynamical systems theory to applications, Journal of Physics A: Mathematical and
Theoretical, 46, 250 301, https://doi.org/10.1088/1751-8113/46/25/250301, 2013.

Cencini, M. and Vulpiani, A.: Finite size Lyapunov exponent: review on applications, Journal of Physics A: Mathematical and Theoretical,
46, 254 019, https://doi.org/10.1088/1751-8113/46/25/254019, 2013.

De Cruz, L., Schubert, S., Demaeyer, J., Lucarini, V., and Vannitsem, S.: Exploring the Lyapunov instability properties of high-dimensional
atmospheric and climate models, Nonlinear Processes in Geophysics, 25, 387–412, https://doi.org/10.5194/npg-25-387-2018, 2018a.

De Cruz, L., Schubert, S., Demaeyer, J., Lucarini, V., and Vannitsem, S.: Exploring the Lyapunov instability properties of high-dimensional
atmospheric and climate models, Nonlinear Processes in Geophysics, 25, 387–412, https://doi.org/10.5194/npg-25-387-2018, 2018b.

Eckmann, J. P. and Ruelle, D.: Ergodic theory of chaos and strange attractors, Rev. Mod. Phys., 57, 617–656,
https://doi.org/10.1103/RevModPhys.57.617, 1985.

Evensen, G.: Data assimilation: the ensemble Kalman filter, Springer Science & Business Media, 2009.

Faranda, D., Messori, G., and Yiou, P.: Dynamical proxies of North Atlantic predictability and extremes, Scientific Reports, 7, 41 278,
https://doi.org/10.1038/srep41278, 2017.

Froyland, G., Hüls, T., Morriss, G. P., and Watson, T. M.: Computing covariant Lyapunov vectors, Oseledets vectors, and dichotomy projectors: A comparative numerical study, Physica D: Nonlinear Phenomena, 247, 18–39, https://doi.org/https://doi.org/10.1016/j.physd.2012.12.005, 2013.

Gálfi, V. M., Bódai, T., and Lucarini, V.: Convergence of Extreme Value Statistics in a Two-Layer Quasi-Geostrophic Atmospheric Model, Complexity, 2017, 5340 858, https://doi.org/10.1155/2017/5340858, 2017.

Gallavotti, G. and Lucarini, V.: Equivalence of non-equilibrium ensembles and representation of friction in turbulent flows: the Lorenz 96 model, Journal of Statistical Physics, 156, 1027–1065, 2014.

Ginelli, F., Poggi, P., Turchi, A., Chaté, H., Livi, R., and Politi, A.: Characterizing Dynamics with Covariant Lyapunov Vectors, Phys. Rev. Lett., 99, 130 601, https://doi.org/10.1103/PhysRevLett.99.130601, 2007.

Grudzien, C., Carrassi, A., and Bocquet, M.: Asymptotic forecast uncertainty and the unstable subspace in the presence of additive model error, SIAM/ASA Journal on Uncertainty Quantification, 6, 1335–1363, 2018a.

Grudzien, C., Carrassi, A., and Bocquet, M.: Chaotic dynamics and the role of covariance inflation for reduced rank Kalman filters with model error, Nonlinear Processes in Geophysics, 25, 633–648, 2018b.

Holton, J. R. and Hakim, G. J.: An Introduction to Dynamic Meteorology, 4th ed., Academic Press, San Diego, CA, 2013.

Kalnay, E.: Atmospheric Modeling, Data Assimilation and Predictability, Cambridge University Press, https://doi.org/10.1017/CBO9780511802270, 2002.

Kuptsov, P. V. and Parlitz, U.: Theory and computation of covariant Lyapunov vectors, Journal of nonlinear science, 22, 727–762, 2012.

Lai, Y.-C.: Unstable dimension variability and complexity in chaotic systems, Phys. Rev. E, 59, R3807–R3810, https://doi.org/10.1103/PhysRevE.59.R3807, 1999.

Lorenz, E. N.: Available Potential Energy and the Maintenance of the General Circulation, Tellus, 7, 157–167, https://doi.org/10.1111/j.2153-3490.1955.tb01148.x, 1955.

Lorenz, E. N.: Deterministic nonperiodic flow, Journal of the atmospheric sciences, 20, 130–141, 1963.

Lorenz, E. N.: Predictability: A problem partly solved, in: Proc. Seminar on predictability, vol. 1, 1996.

Lucarini, V. and Gritsun, A.: A new mathematical framework for atmospheric blocking events, Climate Dynamics, 54, 575–598, 2020.

Lucarini, V., Faranda, D., Wouters, J., and Kuna, T.: Towards a General Theory of Extremes for Observables of Chaotic Dynamical Systems, Journal of Statistical Physics, 154, 723–750, https://doi.org/10.1007/s10955-013-0914-6, 2014.

Lucarini, V., Faranda, D., de Freitas, A. C. G. M. M., de Freitas, J. M. M., Holland, M., Kuna, T., Nicol, M., Todd, M., and Vaienti, S.: Extremes and Recurrence in Dynamical Systems, Wiley, New York, 2016.

Maclean, J. and Van Vleck, E. S.: Particle filters for data assimilation based on reduced-order data models, Quarterly Journal of the Royal Meteorological Society, 147, 1892–1907, 2021.

Messori, G., Caballero, R., and Faranda, D.: A dynamical systems approach to studying midlatitude weather extremes, Geophysical Research Letters, 44, 3346–3354, https://doi.org/https://doi.org/10.1002/2017GL072879, 2017.

Miller, R. N., Ghil, M., and Gauthiez, F.: Advanced data assimilation in strongly nonlinear dynamical systems, Journal of Atmospheric Sciences, 51, 1037–1056, 1994.

Palatella, L., Carrassi, A., and Trevisan, A.: Lyapunov vectors and assimilation in the unstable subspace: theory and applications, Journal of Physics A: Mathematical and Theoretical, 46, 254 020, 2013.

Palmer, T. N. and Zanna, L.: Singular vectors, predictability and ensemble forecasting for weather and climate, Journal of Physics A: Mathematical and Theoretical, 46, 254 018, https://doi.org/10.1088/1751-8113/46/25/254018, 2013.

Pikovsky, A. and Politi, A.: Lyapunov Exponents: A Tool to Explore Complex Dynamics, Cambridge University Press, https://doi.org/10.1017/CBO9781139343473, 2016.

Ruelle, D.: Ergodic theory of differentiable dynamical systems, Publications Mathématiques de l'Institut des Hautes Études Scientifiques,
570   50, 27–58, https://doi.org/10.1007/BF02684768, 1979.

Schubert, S. and Lucarini, V.: Covariant Lyapunov vectors of a quasi-geostrophic baroclinic model: analysis of instabilities and feedbacks, Quarterly Journal of the Royal Meteorological Society, 141, 3040–3055, https://doi.org/https://doi.org/10.1002/qj.2588, 2015.

Tondeur, M., Carrassi, A., Vannitsem, S., and Bocquet, M.: On temporal scale separation in coupled data assimilation with the ensemble kalman filter, Journal of Statistical Physics, pp. 1–25, 2020.

575 Trevisan, A. and Pancotti, F.: Periodic Orbits, Lyapunov Vectors, and Singular Vectors in the Lorenz System, Journal of the Atmospheric Sciences, 55, 390 – 398, https://doi.org/10.1175/1520-0469(1998)055<0390:POLVAS>2.0.CO;2, 1998.

Van Leeuwen, P. J., Künsch, H. R., Nerger, L., Potthast, R., and Reich, S.: Particle filters for high-dimensional geoscience applications: A review, Quarterly Journal of the Royal Meteorological Society, 145, 2335–2365, 2019.

Vannitsem, S.: Predictability of large-scale atmospheric motions: Lyapunov exponents and error dynamics, Chaos: An Interdisciplinary
580   Journal of Nonlinear Science, 27, 032 101, https://doi.org/10.1063/1.4979042, 2017.

Vannitsem, S. and Lucarini, V.: Statistical and dynamical properties of covariant lyapunov vectors in a coupled atmosphere-ocean model—multiscale effects, geometric degeneracy, and error dynamics, Journal of Physics A: Mathematical and Theoretical, 49, 224 001, 2016a.

Vannitsem, S. and Lucarini, V.: Statistical and dynamical properties of covariant lyapunov vectors in a coupled atmosphere-ocean
585   model—multiscale effects, geometric degeneracy, and error dynamics, Journal of Physics A: Mathematical and Theoretical, 49, 224 001, https://doi.org/10.1088/1751-8113/49/22/224001, 2016b.

Vissio, G. and Lucarini, V.: Mechanics and thermodynamics of a new minimal model of the atmosphere, The European Physical Journal Plus, 135, 1–21, 2020.

Wolfe, C. L. and Samelson, R. M.: An efficient method for recovering Lyapunov vectors from singular vectors, Tellus A: Dynamic Meteo-
590   rology and Oceanography, 59, 355–366, https://doi.org/10.1111/j.1600-0870.2007.00234.x, 2007.